

PAPER • OPEN ACCESS

# A green synthesis of $\text{CuInS}_2/\text{MIL-101}(\text{Cr})$ nanocomposite with efficient visible light induced photocatalytic activity

To cite this article: Hong Van T Nguyen *et al* 2023 *Mater. Res. Express* **10** 085506

View the [article online](#) for updates and enhancements.

## You may also like

- [Metal-organic framework structures: adsorbents for natural gas storage](#)  
Aslan Yu. Tsivadze, Oleg E. Aksyutin, Alexander G. Ishkov et al.
- [Synthesis of MIL-101\(Cr\) Metal Organic Framework by Green Synthesis for  \$\text{CO}\_2\$  Gas Adsorption](#)  
Pui San Ho, Kok Chung Chong, Soon Onn Lai et al.
- [Synthesis of  \$\text{Fe}\_3\text{O}\_4\$ @MIL-101\(Fe\) for a Novel Electrochemistry Detection of Citric Acid](#)  
Shuqi Zhou, Tao Liang, Chiyu Ma et al.

# Materials Research Express



## PAPER

# A green synthesis of CuInS<sub>2</sub>/MIL-101(Cr) nanocomposite with efficient visible light induced photocatalytic activity

### OPEN ACCESS

RECEIVED  
8 June 2023

REVISED  
28 July 2023



ACCEPTED FOR PUBLICATION  
17 August 2023

PUBLISHED  
29 August 2023

Original content from this work may be used under the terms of the [Creative Commons Attribution 4.0 licence](#).

Any further distribution of this work must maintain attribution to the author(s) and the title of the work, journal citation and DOI.



Hong Van T Nguyen<sup>1,2</sup>, Manh B Nguyen<sup>1,3</sup>, Huan V Doan<sup>4,5</sup>  and Xuan Nui Pham<sup>4</sup> 

<sup>1</sup> Graduate University of Science and Technology, Vietnam Academy of Science and Technology, 18 Hoang Quoc Viet street, Cau Giay, Ha Noi, Vietnam

<sup>2</sup> Institute of Environment, Vietnam Maritime University, 484 Lach Tray, Le Chan, Hai Phong, Vietnam

<sup>3</sup> Institute of Chemistry, Vietnam Academy of Science and Technology, 18 Hoang Quoc Viet street, Cau Giay, Ha Noi, Vietnam

<sup>4</sup> Department of Chemical Engineering, Hanoi University of Mining and Geology, 18 Pho Vien, Duc Thang, Bac Tu Liem District, Hanoi, Vietnam

<sup>5</sup> Department of Mechanical Engineering, University of Bristol, Bristol BS8 1TH, United Kingdom

E-mail: [phamxuannui@hmg.edu.vn](mailto:phamxuannui@hmg.edu.vn)

**Keywords:** CuInS<sub>2</sub>, MIL-101(Cr), recycled TPA, plastic recycling, tetracycline degradation

## Abstract

This study demonstrates the sustainable synthesis of multifunctional CIS@MIL-101(Cr) composites for water treatment applications. The composites were prepared via hybridization of CuInS<sub>2</sub> with MIL-101(Cr) resulting in the formation of CIS nanoplates incorporated into MIL-101(Cr). The composites exhibited enhanced visible light photocatalytic activity due to their low bandgap energy and were tested for tetracycline photodegradation achieving a degradation efficiency of 98.8%. The material showed high stability after four cycles, and the effects of reactive species on photodegradation were investigated. The kinetics and mechanism of the photocatalytic process were studied, and LC-MS analysis was conducted to identify intermediate products. These results demonstrate the potential of using waste PET to create new semiconductors for water pollution control, promoting a circular material pathway.

## 1. Introduction

Tetracycline (TC) antibiotics are one of the primarily antibiotics groups used for veterinary purposes, for human therapy and for agricultural purposes due to its broad-spectrum activity, high effectiveness, and reasonable cost [1, 2]. However, it is linked to the difficult metabolization of TC in the human and animal digestion system and, therefore, excreted into the environment by human feces and animal excreta up to 50%–80% [3]. In addition, due to their extensive usage and poor degradation, TC residues in water source has become a serious threat to the environment. Tetracycline is capable of accumulating along the food chain, causing toxicity to the microbial community, encouraging the development, and spread of antibiotic resistance, creating threats to drinking and irrigation water, and disrupting microbial flora in the human intestine [1]. Besides, the residual concentrations of such drugs could affect steroidogenic pathway and consequently may cause endocrine disruption of aquatic species. Most of the wastewater treatment plants are not capable of effectively removing the tetracycline antibiotics. Therefore, there is a need to develop alternative processes to remove them from waters. Advanced oxidation processes by photocatalysis have been proposed as alternative methods to ensure higher degradation and mineralization of tetracycline antibiotics are present in waters [2].

Copper Indium Sulfide (CIS), a member of the chalcopyrite family, is a well-known semiconductor material with numerous solid phases, such as the chalcopyrite and wurtzite phases [4–7]. It is common practise to manufacture CIS nanocrystals with a stable phase structure for usage as a light absorber in photocatalysis [5, 6]. Despite its positive features, such as a bandgap of 1.52 eV and low toxicity, CIS has disadvantages such as poor surface area, low chemical stability, and aggregation during reaction processes. To circumvent these constraints, researchers have combined CIS with other materials to broaden the spectral range of activity and enhance the light-absorbing properties of solar cell materials. Fakhri *et al* [8], for instance, integrated CIS with ZnO to extend

the spectral range of photocatalytic activity to visible light, whereas Zhang *et al* [9] reported on ZnS–CIS nanocomposites, which demonstrated improved performance in the photodegradation of Rhodamine B. Nakamura *et al* [8, 10] enhanced the crystallinity and energy gap of CIS by doping it onto zinc and/or altering it with gallium and/or selenium. In addition, Florent *et al* [11] reported the utilization of g-C<sub>3</sub>N<sub>4</sub> films produced on polycrystalline CIS chalcopyrite electrodes for the generation of hydrogen by photoelectrochemical water splitting. These investigations illustrate the possibility of combining CIS with other materials to improve its photocatalytic activity in a variety of applications.

Metal–organic frameworks (MOFs) have gained significant attention as potentially useful materials for a wide range of applications, including photocatalysis [12–14]. Among them, MIL-101 (MIL, Matériel Institut Lavoisier), specifically chromium terephthalate MOF, has been studied as a potential candidate for photocatalysis due to its remarkable moisture stability, significant thermal stability, ample pore volume and surface area, and numerous unsaturated chromium sites [15–18]. Several studies have concentrated on the integration of CIS with MIL-101(Cr) to enhance its photocatalytic efficacy. For example, Zhang *et al* [19] documented the successful fabrication of ZnS–CIS nanocrystals on MIL-101(Cr) with increased Rhodamine B (RB) photodegradation activity. The researchers ascribed the increased performance to the collaborative impact of the composite structure of ZnS–CIS/MIL-101(Cr), which created a larger surface area for the adsorption of RB molecules and facilitated electron transfer between CIS and ZnS. Similarly, Yang *et al* [20] reported the synthesis of a CuInS<sub>2</sub>/MIL-101(Cr) composite for efficient photocatalytic hydrogen evolution. The authors credit the better performance of the composite to the increased absorption of visible light and better separation of electrons and holes, which result from the interaction between CuInS<sub>2</sub> and MIL-101(Cr). These studies highlight the potential of integrating CIS with MOFs, particularly MIL-101(Cr), for photocatalytic applications. The synergistic effect of the composite structure can intensify the absorption of visible light, enhance the separation of electrons and holes, and expand the specific surface area, leading to an improvement in photocatalytic effectiveness.

Terephthalic acid (TPA) is an important component in the production of MOFs. However, TPA is primarily generated from petroleum-based sources, which presents sustainability and environmental impact problems. To solve this issue, researchers have investigated the use of recycled TPA produced from waste polyethylene terephthalate (PET) for MOF production [21–24]. Several studies have reported the successful synthesis of MOFs using recycled TPA [25, 26]. Lo *et al* [27] described the facile and scalable production of nanoporous MOFs from PET waste. Comparing the properties of the MOFs synthesized from recycled TPA to those synthesized from commercial TPA, the scientists established the practicality of employing recycled TPA. The results demonstrated that the MOFs synthesized from recycled TPA possessed comparable characteristics to those synthesized from commercial TPA, showing the viability of employing recycled TPA as a renewable source. The researchers demonstrated that the MOF created using recycled TPA possessed comparable characteristics to those produced from commercial TPA, including a high surface area, significant pore volume, and outstanding thermal stability. These experiments illustrate the viability of using recycled TPA for MOF synthesis as a sustainable resource. By employing waste PET and other sources of TPA, researchers can lessen their dependency on petroleum-based supplies and contribute to a more sustainable and eco-friendly method of MOF synthesis.

This investigation aimed to develop an environmentally friendly method for synthesizing the CIS@MIL-101(Cr) nanoarchitecture and evaluate its ability to degrade tetracycline (TC) through photocatalysis. MIL-101(Cr) was used as a substrate to enhance the dispersion of CIS, resulting in improved performance of both materials. The structure of the hybrid nanocomposite and its relationship with photocatalytic activity were discussed. Additionally, the kinetics of TC degradation and the photocatalytic reaction of the hybrid nanocomposite were proposed. All in all, this research showcases the possibility of utilizing CIS@MIL-101(Cr) nanocomposites as effective photocatalysts for the disintegration of TC and other contaminants. The use of a sustainable synthesis approach and the enhancement of the performance of both materials make this nanocomposite a promising candidate for various photocatalytic applications.

## 2. Experimental

### 2.1. Materials

Polyethylene terephthalate (PET), ethylene glycol (EG, 99%), sodium hydroxide (NaOH, 98%), sulfuric acid (H<sub>2</sub>SO<sub>4</sub>, 98%), chromium(III) nitrate nonahydrate (Cr(NO<sub>3</sub>)<sub>3</sub>·9H<sub>2</sub>O, 99%), hydrofluoric acid (HF, 48%), ethanol (C<sub>2</sub>H<sub>5</sub>OH, 99%), dimethylformamide (DMF, 98%), copper(I) iodide, sodium dodecyl sulfate (C<sub>12</sub>H<sub>25</sub>O<sub>4</sub>S), thioacetamide (CH<sub>3</sub>CSNH<sub>2</sub>, 98%), indium(III) chloride (InCl<sub>3</sub>, 98%), hydrochloric acid (HCl, 37%), 1,4–benzoquinon (BQ, 99%), *tert*-butyl alcohol (TBA, 99%). TPA was recovered from polyethylene

terephthalate (PET) according to our previous study [24, 25]. Chemicals in the work were purchased by Sigma–Aldrich and used without further purification.

## 2.2. Synthesis of CIS

The synthesis of tetragonal chalcopyrite CIS nanoparticles via a solvothermal method is described. Firstly, 1.4419 g of sodium dodecyl sulfate (5 mmol) was dissolved in 25 ml of ethylene glycol in a flask and heated at 70 °C for 15 min. Next, a solution of 1 mmol CuI, 1 mmol InCl<sub>3</sub>, and 5 mmol thioacetamide was added to the above solution, and heating was continued for 30 min to form a homogeneous solution. The resulting solution was then placed in a Teflon flask in an autoclave and hydrothermally treated at 180 °C for 24 h. The formed dark solid, CIS, was thoroughly washed with distilled water and ethanol before being dried at 80 °C for 5 h.

## 2.3. Synthesis of CIS@MIL-101(Cr)

To synthesize CIS@MIL-101(Cr) composite, 0.404 g of CIS and 4 g of Cr(NO<sub>3</sub>)<sub>3</sub>·9H<sub>2</sub>O were dispersed in 20 ml of deionized water using a magnetic stirrer for 30 min, followed by sonication for 60 min to form a homogeneous solution. Next, 1.142 g of TPA, 0.43 ml of HF, and 25 ml of H<sub>2</sub>O were added to the solution, and stirring was continued for 30 min. The resulting solution was sonicated for 30 min at room temperature and then placed in a Teflon-lined stainless-steel autoclave to enhance the attachment of the materials. The autoclave was heated to 180 °C for 12 h. The resulting sample was filtered and washed with DMF at 100 °C for 1 h and with C<sub>2</sub>H<sub>5</sub>OH at 80 °C for 12 h to completely remove impurities. Finally, the sample was dried at 80 °C to obtain the CIS@MIL-101(Cr) composite.

## 2.4. Photocatalytic activity tests

To evaluate the photocatalytic performance of the CIS@MIL-101(Cr) nanocomposite, the degradation of TC under a 60 W Xenon lamp was investigated. Cut-off filters were used to remove the light range of  $\lambda < 420$  nm and simulate visible light. In the experiment, 50 mg of the synthesized photocatalyst was homogeneously dispersed into a 100 ml TC aqueous solution (50 mg l<sup>-1</sup>). Before irradiating light, the suspension was stirred under dark conditions for 60 min to attain an adsorption–desorption equilibrium state. After light irradiation, 2 ml of the suspension was taken and centrifuged. The clear solution was analyzed by UV–vis spectrophotometry at the maximum absorption wavelength of 357 nm. The photodegradation efficiency was calculated using the following equation:

$$\text{Photodegradation efficiency(\%)} = \frac{C_0 - C_t}{C_0} \times 100\% \quad (1)$$

where  $C_0$  is the initial concentration of TC, and  $C_t$  is the concentration of TC after light irradiation.

To investigate the photocatalytic degradation kinetics of the CIS@MIL-101(Cr) nanocomposite, both pseudo-first-order and pseudo-second-order reactions were evaluated using equations (2) and (3):

$$\ln\left(\frac{C_0}{C_t}\right) = k_1 t \quad (2)$$

$$\frac{1}{C_t} - \frac{1}{C_0} = k_2 t \quad (3)$$

where  $k_1$  and  $k_2$  are the pseudo-first-order rate constant and the pseudo-second-order rate constant (min<sup>-1</sup>), respectively. Trapping experiments were also conducted to determine the reactive species involved in the photocatalytic degradation process. In each experiment, 50 mg of CIS@MIL-101(Cr) was added to 100 ml of TC solution (50 mg l<sup>-1</sup>), followed by the addition of 2 mm of tert-butyl alcohol (TBA), 1,4-benzoquinone (BQ), ammonium oxalate monohydrate (AO), or potassium dichromate (K<sub>2</sub>Cr<sub>2</sub>O<sub>7</sub>) to the suspension. TBA was used for hydroxyl radical ( $\bullet$ OH) scavenging, while BQ was used for superoxide radical ( $\bullet$ O<sub>2</sub><sup>-</sup>) scavenging, AO for holes ( $h^+$ ) scavenging, and K<sub>2</sub>Cr<sub>2</sub>O<sub>7</sub> for electrons ( $e^-$ ) scavenging.

## 2.5. Characterization

The synthesized materials were characterized using various techniques. The crystal structures and phases were determined by powder x-ray diffraction (XRD) using a Bruker, Germany system with CuK $\alpha$  radiation,  $\lambda = 0.154$  nm, and a scanning rate of 3°/min. The size distribution, surface, and morphology were analyzed using a scanning electron microscope (SEM-4800, Hitachi) and transmission electron microscope (TEM, JEM-2100F, JEOL, Japan). Fourier transform infrared spectra (FT-IR) and Raman scattering were measured using an FT-IR Affinity-1S (SHIMADZU) and MacroRAM/Horiba model, respectively, with a laser at 785 nm. X-ray energy dispersion (EDX) and EDX mapping were carried out using a JED-2300 with a gold coating. Optical characterizations were recorded by UV–vis diffuse reflectance spectroscopy (DRS-UV) using a UV-2600 spectrophotometer (Shimadzu) and photoluminescence (PL) spectra using a Cary Eclipse fluorescence

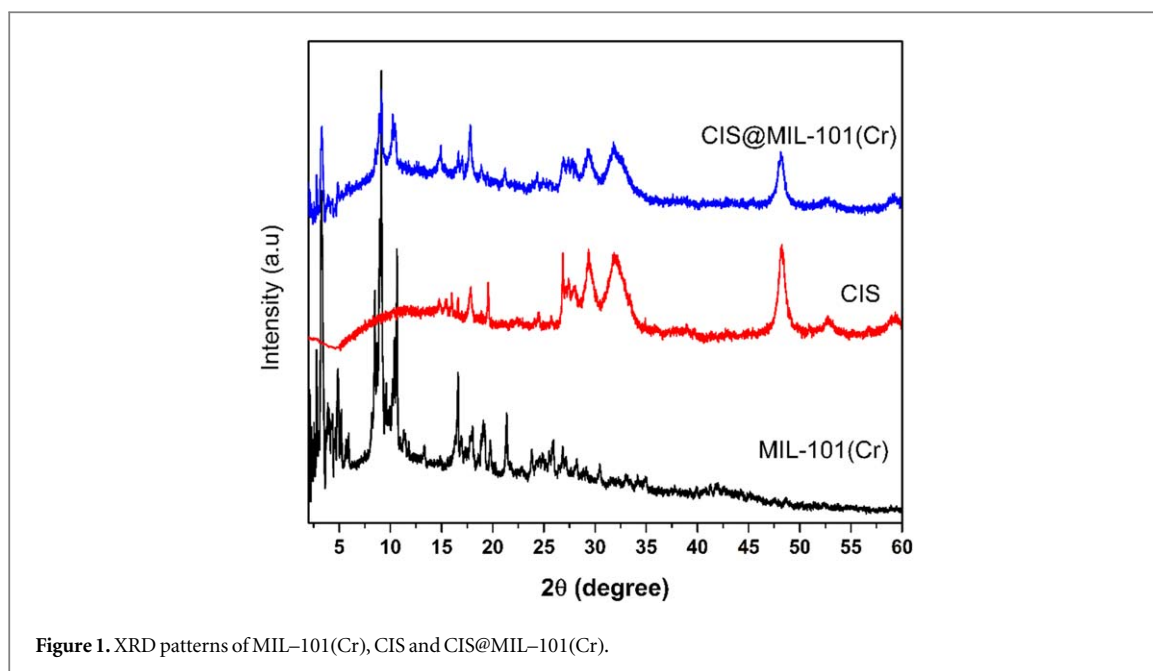


Figure 1. XRD patterns of MIL-101(Cr), CIS and CIS@MIL-101(Cr).

spectrophotometer (Varian). The Brunauer–Emmett–Teller (BET) specific surface area was determined at liquid–nitrogen temperature (77 K) using the  $N_2$  adsorption–desorption technique on a ChemBET–3030 system. X–ray photoelectron spectroscopy (XPS) was conducted using an ESCALab 250 spectrometer (Thermo VG, UK).

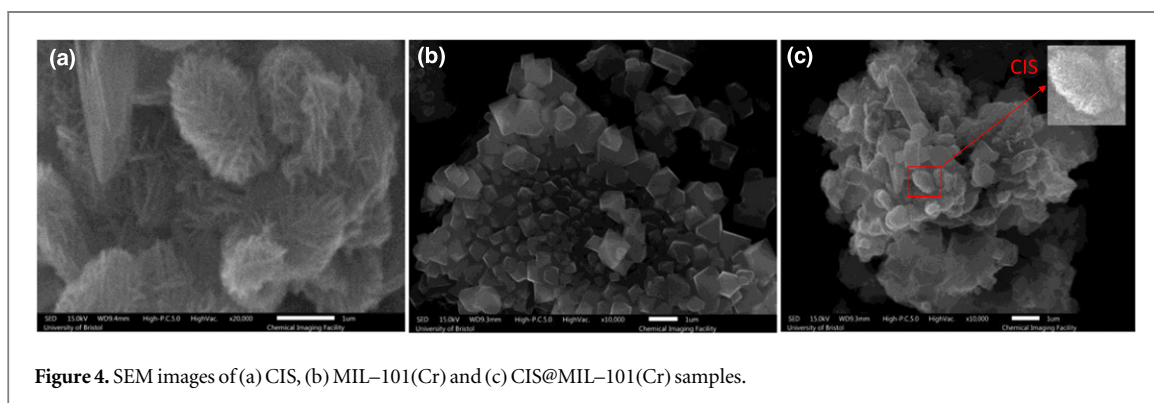
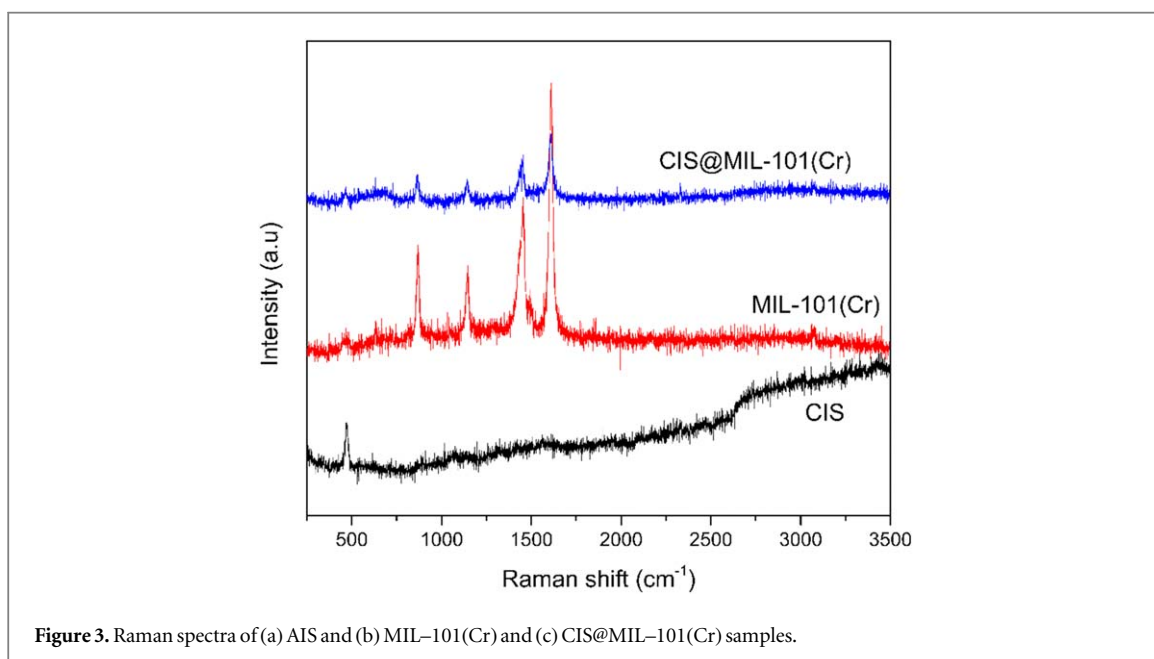
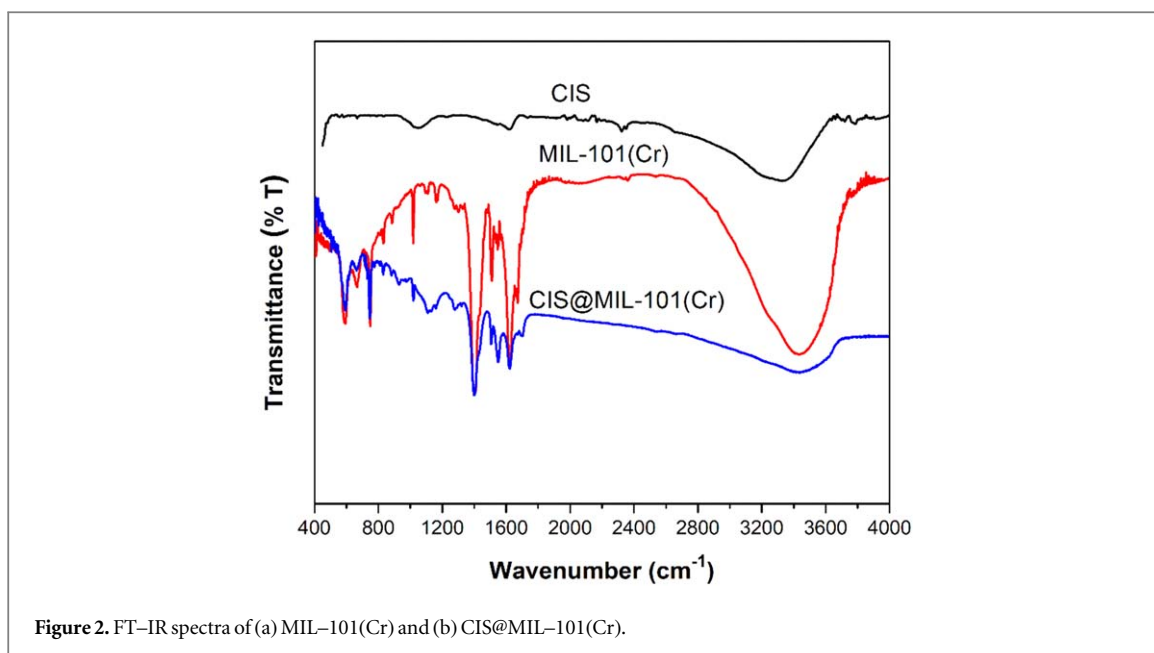
### 3. Results and discussion

#### 3.1. Characterization of samples

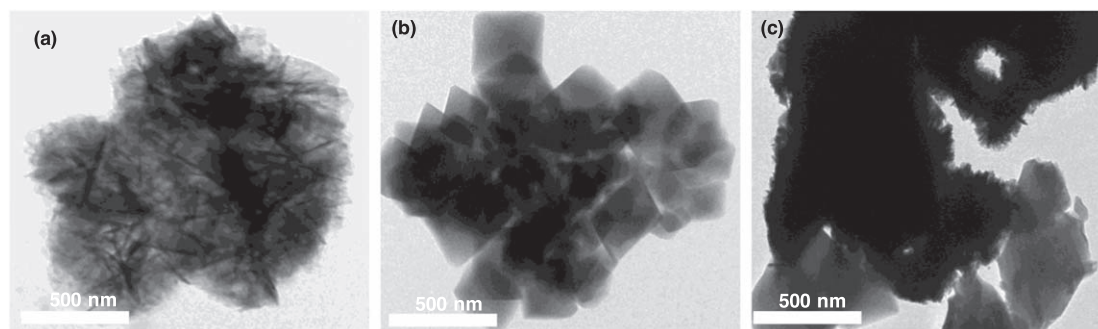
Figure 1 illustrates the x–ray diffraction (XRD) patterns of CIS, MIL–101(Cr), and CIS@MIL–101(Cr). The CIS sample was synthesized via solvothermal treatment at 180 °C, and exhibits intense diffraction peaks at 27.98°/29.10°, 32.55°, and 50.32°/54.96° degrees  $2\theta$ , which can be indexed as (112), (103), and (204/224) and (116/312) planes reflections of the chalcopyrite tetragonal structure (JCPDS card No 85-1575). The XRD spectra of MIL-101(Cr) exhibited diffraction peaks at  $2\theta = 3.29^\circ, 4.83^\circ, 5.81^\circ, 8.52^\circ, 9.04^\circ,$  and  $10.65^\circ$ , which corresponded to the crystal planes of (311), (400), (511), (822), (753) and (1022) in MIL–101(Cr), respectively [27]. The presence of small peaks near  $2\theta = 25.2^\circ$  and/or  $27.9^\circ$  confirmed the effective elimination of excess terephthalic acid crystals from the pores of MIL–101(Cr) [28, 29]. The XRD patterns of the hybrid substance indicated that the major peaks of both MIL–101(Cr) and CIS remained detectable, but their peak intensities were weakened as a result of the emergence of defects and the notable decline of the lattice structure after the CIS was added onto the surface and into the pores of the MIL–101(Cr) framework.

Figure 2 illustrates the Fourier transform infrared (FT–IR) spectra of MIL–101(Cr) and CIS@MIL–101(Cr). The O–C–O stretching vibration was assigned to the characteristic peak at  $1619\text{ cm}^{-1}$ . The C=C vibration was represented by the extension peaks of  $1518\text{ cm}^{-1}$  and  $1399\text{ cm}^{-1}$ . Moreover, the bonds in the aromatic ring were attributed to the vibrational modes within the range of  $600\text{ to }1600\text{ cm}^{-1}$ , such as  $1171, 1017, 887,$  and  $750\text{ cm}^{-1}$  [29, 30]. Another notable peak at around  $580\text{ cm}^{-1}$  was associated with the Cr–O stretching mode, indicating the successful bonding between the metal ion ( $\text{Cr}^{3+}$ ) and (–COO) groups of TPA. The main peaks of MIL–101(Cr) were still observable in the CIS@MIL–101(Cr) composite [31]. The presence of characteristic peaks of individual components in the spectrum of the composite partly proved their combination, each of them was not eliminated during the reaction.

Figure 3 presents the Raman spectra of the pristine CIS, MIL–101(Cr), and CIS@MIL–101(Cr) nanocomposite, which were utilized to confirm their crystal structures. The Raman spectrum of the nanohybrid substance exhibited the characteristic bands of MIL–101 porous material [32]. In pure CIS, a chalcopyrite phase was noticeable at  $291\text{ cm}^{-1}$ , and it was linked to the A1 main vibrational band symmetry that arose from the vibration of sulfur anions in the linear plane with copper and indium cations of the initial CIS structure. Remarkably, as the CIS content loaded on MIL–101(Cr) varied, the peak intensities gradually reduced in comparison to those of the original CIS and MIL–101(Cr), suggesting the presence of a strong interaction between CIS and MIL–101(Cr).







**Figure 5.** TEM images of (a) CIS, (b) MIL-101(Cr) and (c) CIS@MIL-101(Cr) samples.

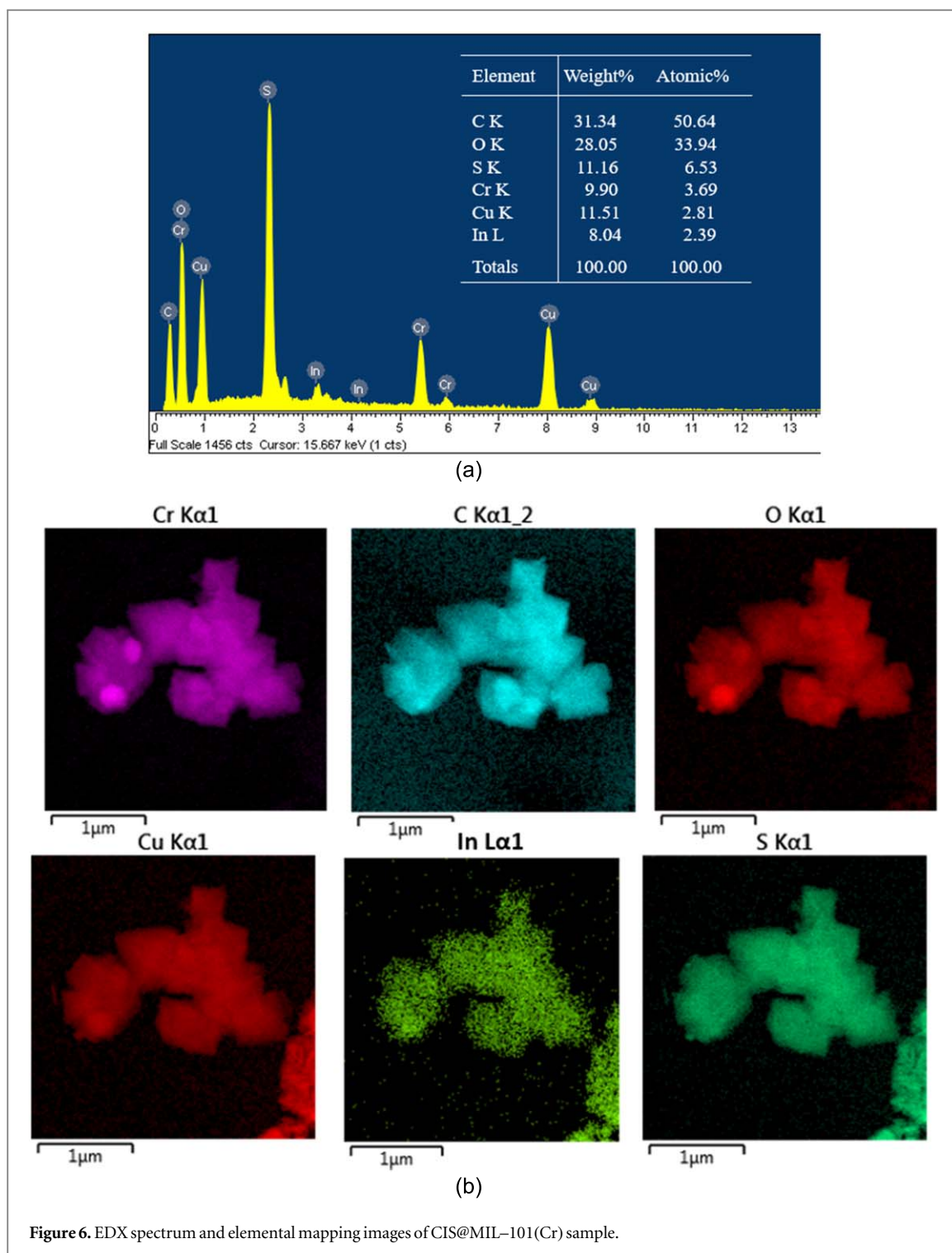
The morphology of the MIL-101(Cr), CIS, and CIS@MIL-101(Cr) samples was evaluated by SEM and TEM (figures 4 and 5, respectively). The SEM image in figure 4(a) displays the typical flowerlike hierarchical structures of pristine CIS. Following the combination of CIS with MIL-101(Cr), the morphology of the CIS flowerlike microspheres with a diameter of 0.5–1.0  $\mu\text{m}$  remained unchanged, which were formed to clusters were also observed (figure 4(c)), indicating the incorporation of the CIS structures into MIL-101(Cr) material, in which had 0.4–0.6  $\mu\text{m}$  particles. Transmission electron microscopy (TEM) was employed to examine the sample structure further, the contours in these sample are corresponding to the surface combination between CIS and nanoparticles MIL-101(Cr). In the figure 5(c), the darker regions on the micrograph can show to the loading of high-density CIS, indicating that MIL-101(Cr) particles were successfully attached to CIS sheets via hydrothermal ‘one pot’ synthesis.

Additionally, the x-ray energy dispersion (EDX) spectrum and element mapping of the CIS@MIL-101(Cr) nanocomposite are shown in figure 6, where the analysis revealed the presence of Cr, C, O, Cu, In, and S elements in a molar ratio of Cu, In, and S approximately 1:1:2, respectively, indicating the stoichiometric composition of  $\text{CuInS}_2$ .

The  $\text{N}_2$  adsorption–desorption method at 77 K was used to determine the pore size and specific surface area of the CIS, MIL-101(Cr), and CIS@MIL-101(Cr) samples, as presented in figure 7. It was observed that the isotherm of MIL-101(Cr) was of type I, while that of CIS@MIL-101(Cr) was of type III. The  $\text{N}_2$  adsorption capacity was high at the low-pressure region, and the hysteresis was of H3 type, indicating that both materials were mesoporous [33]. The surface area, pore volume, and pore size of MIL-101(Cr) were found to be  $1873 \text{ m}^2 \text{ g}^{-1}$ ,  $0.97 \text{ cm}^3 \text{ g}^{-1}$ , and 2.06 nm, respectively (see table 1). However, after combining with CIS, the surface area and pore volume significantly decreased to  $1211 \text{ m}^2 \text{ g}^{-1}$  and  $0.64 \text{ cm}^3 \text{ g}^{-1}$ , respectively. This could be attributed to the nonporous nature of the inner CIS chalcogenide and its higher density. Notably, the pore size of the CIS@MIL-101(Cr) nanocomposite was found to be 2.34 nm, similar to that of pure MIL-101(Cr) crystal. This indicated that the coating of nanospheres on the surface of MIL-101(Cr) provides more surface-active sites for the adsorption and catalysis of reactant molecules.

X-ray photoelectron spectroscopy (XPS) was used to identify the elements and their oxidation states present in the CIS@MIL-101(Cr) sample (figure 8). The XPS full scan spectrum (figure 8(a)) revealed the presence of C, O, S, Cr, In, and Cu in the sample. The C1s spectra of MIL-101(Cr) and CIS@MIL-101(Cr) could be resolved into four peaks at 284.8, 286.4, 288.8, and 290.3 eV, representing the C=C/C–C, C=O, C–O, and O–C=O bonds, respectively [34]. The O1s spectra of the two samples exhibit three peaks at 530.7 eV, 532 eV, and 533.2 eV, corresponding to oxygen in the crystal lattice between metal and oxygen (Cr–O), O–C=O, and chemisorbed oxygen species [35]. The main peaks at 577.4 eV (Cr 2p<sub>1/2</sub>) and 587.4 eV (Cr 2p<sub>3/2</sub>) in figure 8(d) confirm the existence of  $\text{Cr}^{3+}$  in MIL-101(Cr) and CIS@MIL-101(Cr) [36]. The binding energy peaks of  $\text{Cu}^+$  at 932.6 and 952.4 eV, assigned to Cu 2p<sub>1/2</sub> and Cu 2p<sub>3/2</sub> (figure 8(e)), were observed in both CIS and CIS@MIL-101(Cr) samples, with a maximum separation energy level of 19.8 eV [37]. No peak of  $\text{Cu}^{2+}$  was observed, indicating the reduction of  $\text{Cu}^{2+}$  to  $\text{Cu}^+$  during the synthesis process [38]. The binding energies at 445.6 eV and 453.2 eV, attributed to In 3d<sub>5/2</sub> and In 3d<sub>3/2</sub>, respectively (figure 8(f)), confirm the presence of  $\text{In}^{3+}$ . The binding energies of S 2p were detected at 162.4 eV (S 2p<sub>3/2</sub>) and 163.6 eV (S 2p<sub>1/2</sub>), with a maximum separation of 1.2 eV, indicating the presence of  $\text{S}^{2-}$  due to its different binding with Cu and In, respectively [37].

Figure 9 shows the UV–Vis diffuse reflectance spectra (UV–DRS) of the CIS, MIL-101(Cr), and CIS@MIL-101(Cr) samples. The MIL-101(Cr) sample demonstrated two regions of absorption in the UV–vis DRS spectrum: one in the visible light range (440 nm and 590 nm) and the other in the ultraviolet range (230–280 nm) [39]. The absorption spectrum of the CIS sample showed a broad range of light absorption covering both the ultraviolet and visible regions [40]. The CIS@MIL-101(Cr) composite showed an improved



capacity for absorbing visible light. The bandgap energies of the CIS, MIL-101(Cr), and CIS@MIL-101(Cr) samples were determined using the Tauc plot [41]. To estimate the band gap energies of the samples, a line was drawn tangent to the curve intersecting  $h\nu$  in the graph  $(\alpha h\nu)^2$  versus  $h\nu$ . The bandgap energy of CIS and MIL-101(Cr) was about 1.12 eV and 2.31 eV, consistent with the report of Yanhong *et al* [42]. Sample CIS@MIL-101(Cr) had low band gap energy at 2.02 eV allowed the demonstration of photocatalytic activity under light irradiation.

The charge transfer rates of the CIS, MIL-101(Cr) and CIS@MIL-101(Cr) samples were determined by Electrochemical impedance spectroscopy (EIS). In figure 10(a), the Nyquist plot of the CIS sample shows the smallest semicircle, confirming the fastest charge transfer rate [43, 44]. The CIS@MIL-101(Cr) sample has a Nyquist plot with a smaller semicircle than that of the MIL-101(Cr) sample indicating an improved charge transfer rate. This result may be due to the strong interaction between the CIS and MIL-101(Cr) phases [45–47].



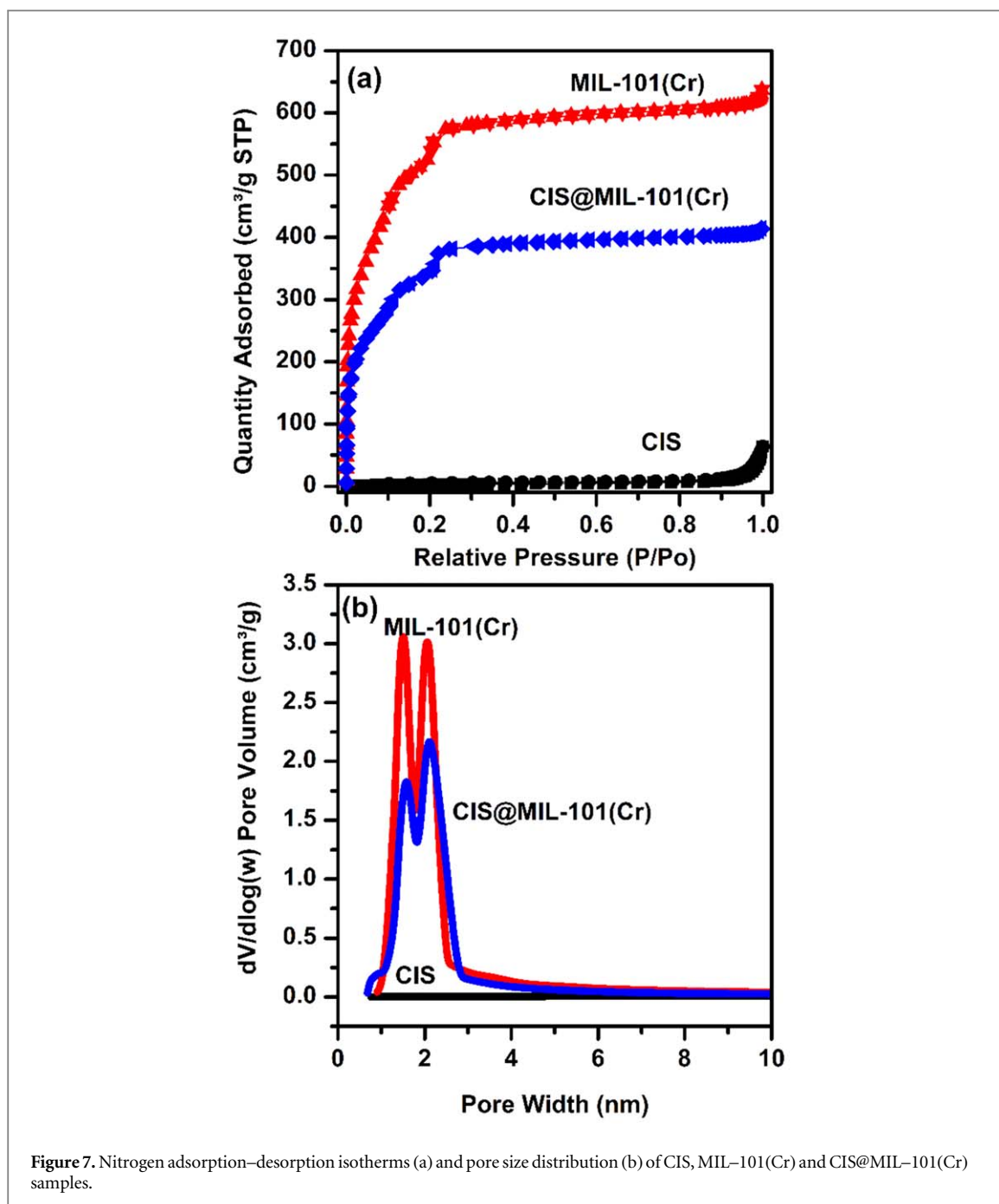
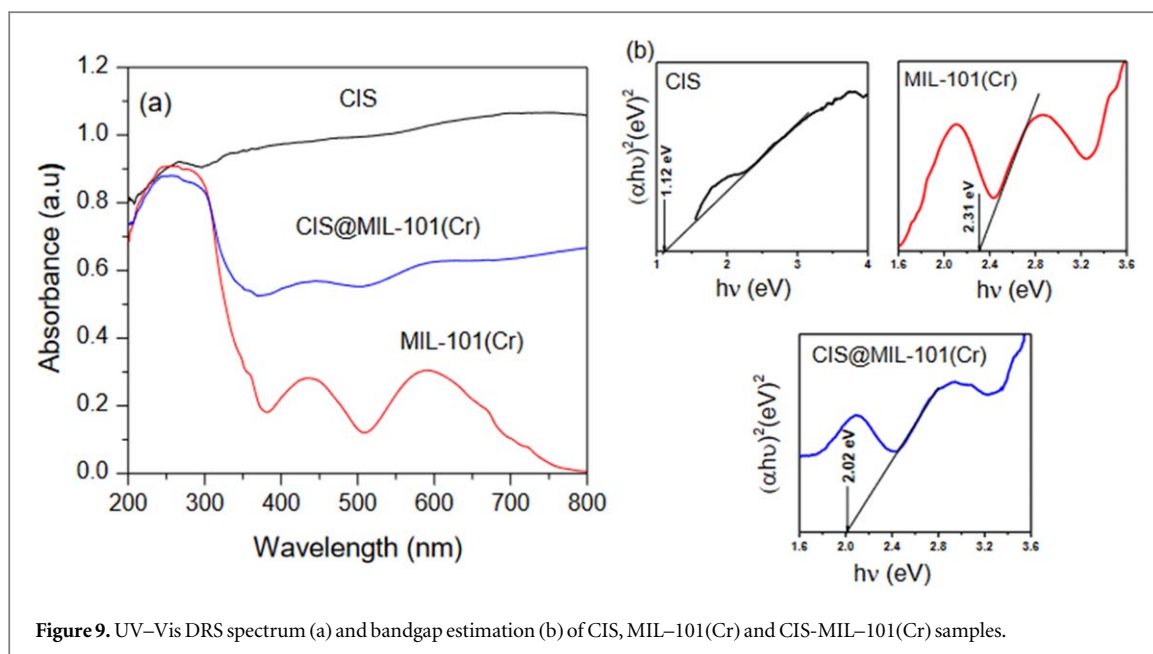
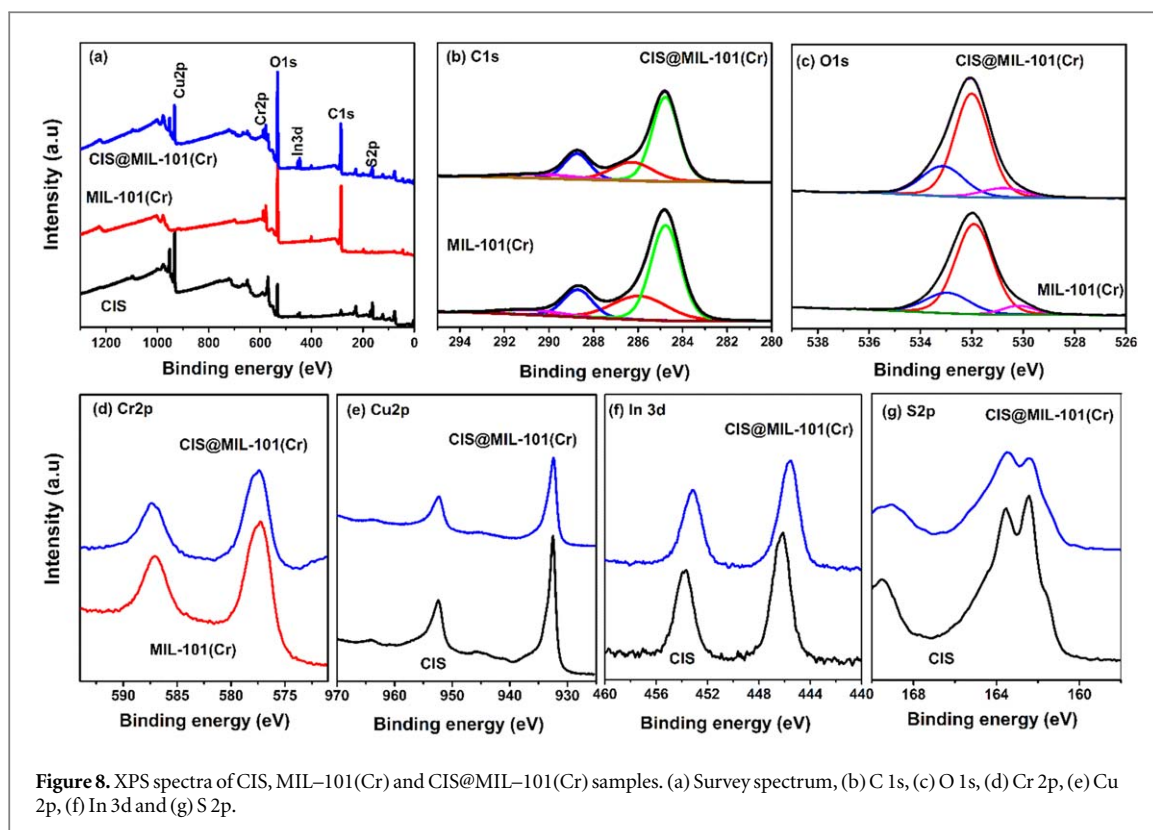


**Table 1.** Textual characteristics of CIS, MIL–101(Cr) and CIS@MIL–101(Cr).

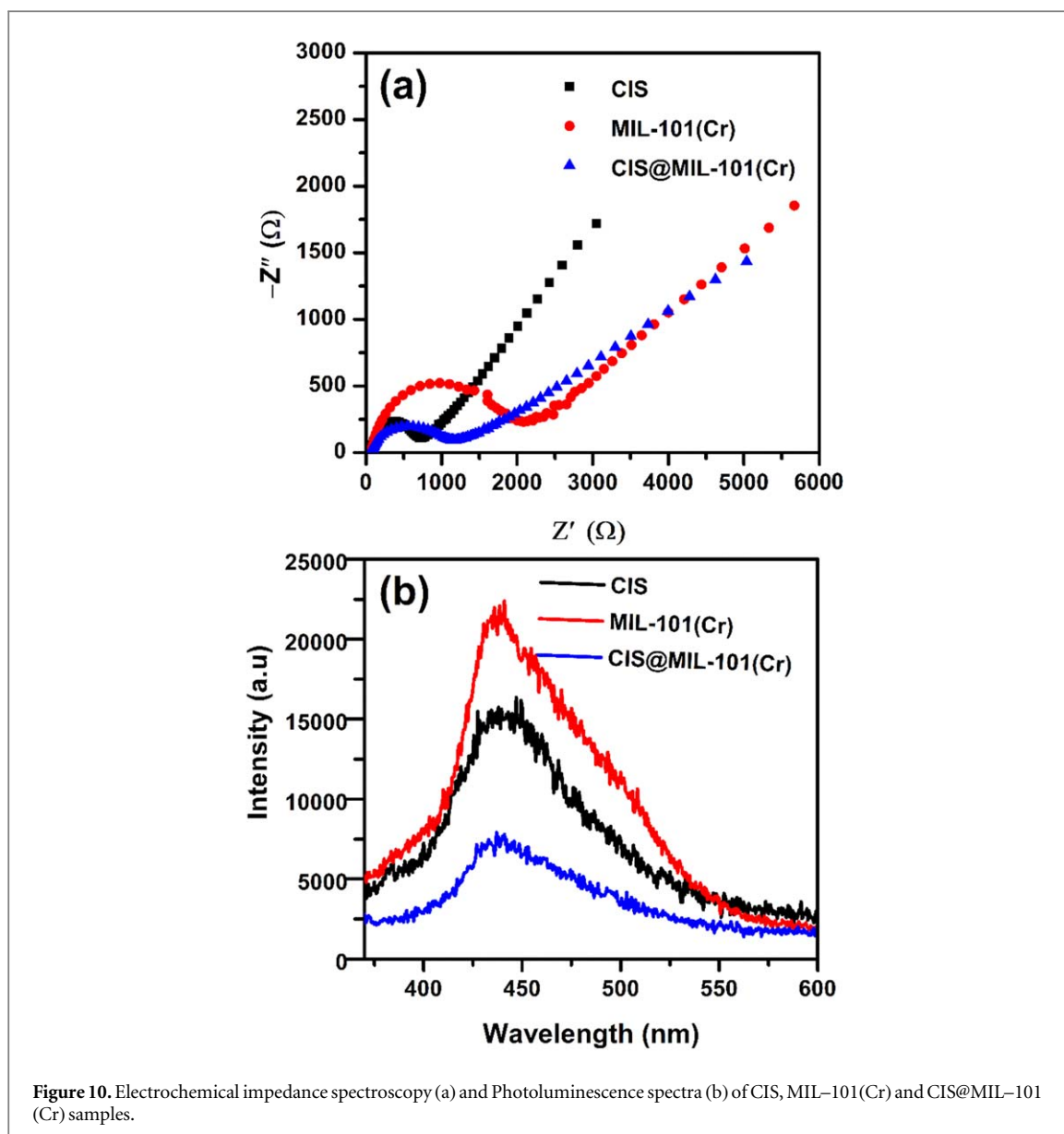
Sample	$S_{\text{BET}}$ ( $\text{m}^2/\text{g}$ )	$V_{\text{pore}}$ ( $\text{cm}^3/\text{g}$ )	$D_{\text{BJH}}$ (nm)
CIS	10.7	0.06	—
MIL–101(Cr)	1873	0.97	2.06
CIS@MIL–101(Cr)	1211	0.64	2.34

Figure 10(b) shows the photoluminescence (PL) spectra of the CIS, MIL–101(Cr), and CIS@MIL–101(Cr) samples. The PL spectrum of the MIL–101(Cr) sample exhibited a wide and intense emission band due to rapid electron–hole recombination [40]. The emission intensity of the CIS@MIL–101(Cr) sample was observed to decrease, suggesting a notable decrease in electron–hole recombination. Furthermore, the peak observed at 436 nm in the original CIS sample shifted to 440 nm in the CIS@MIL–101(Cr) sample, which can be attributed to the trapping of electrons by the defect sites [40].

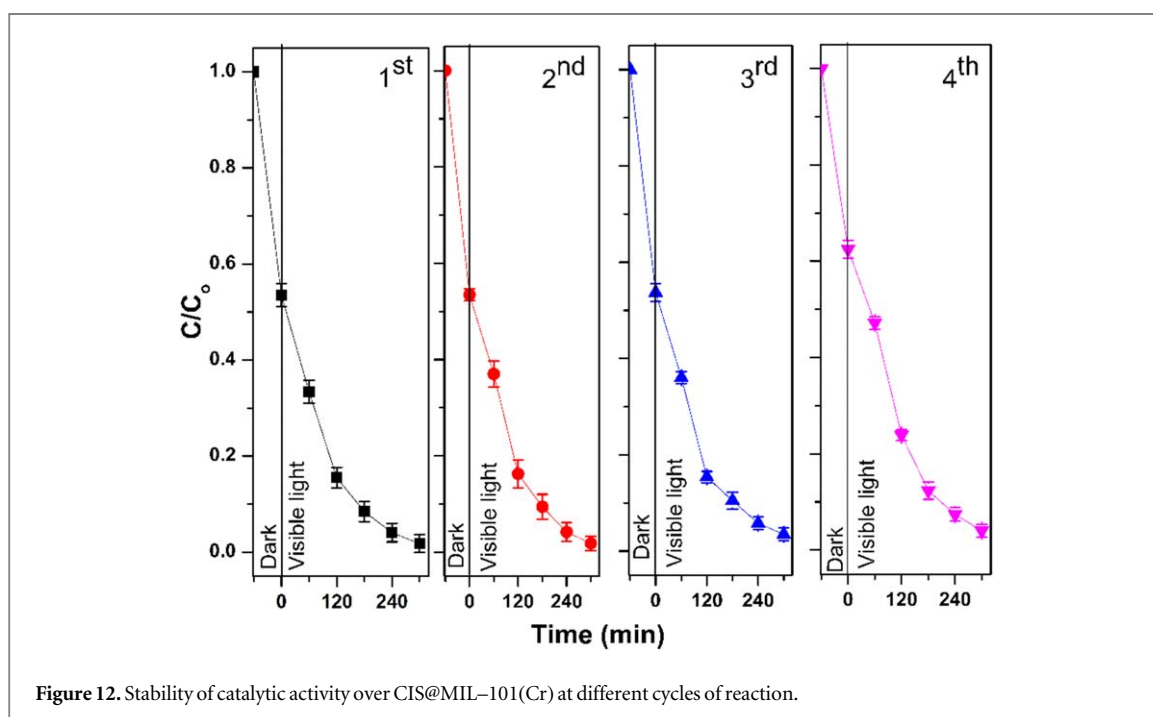
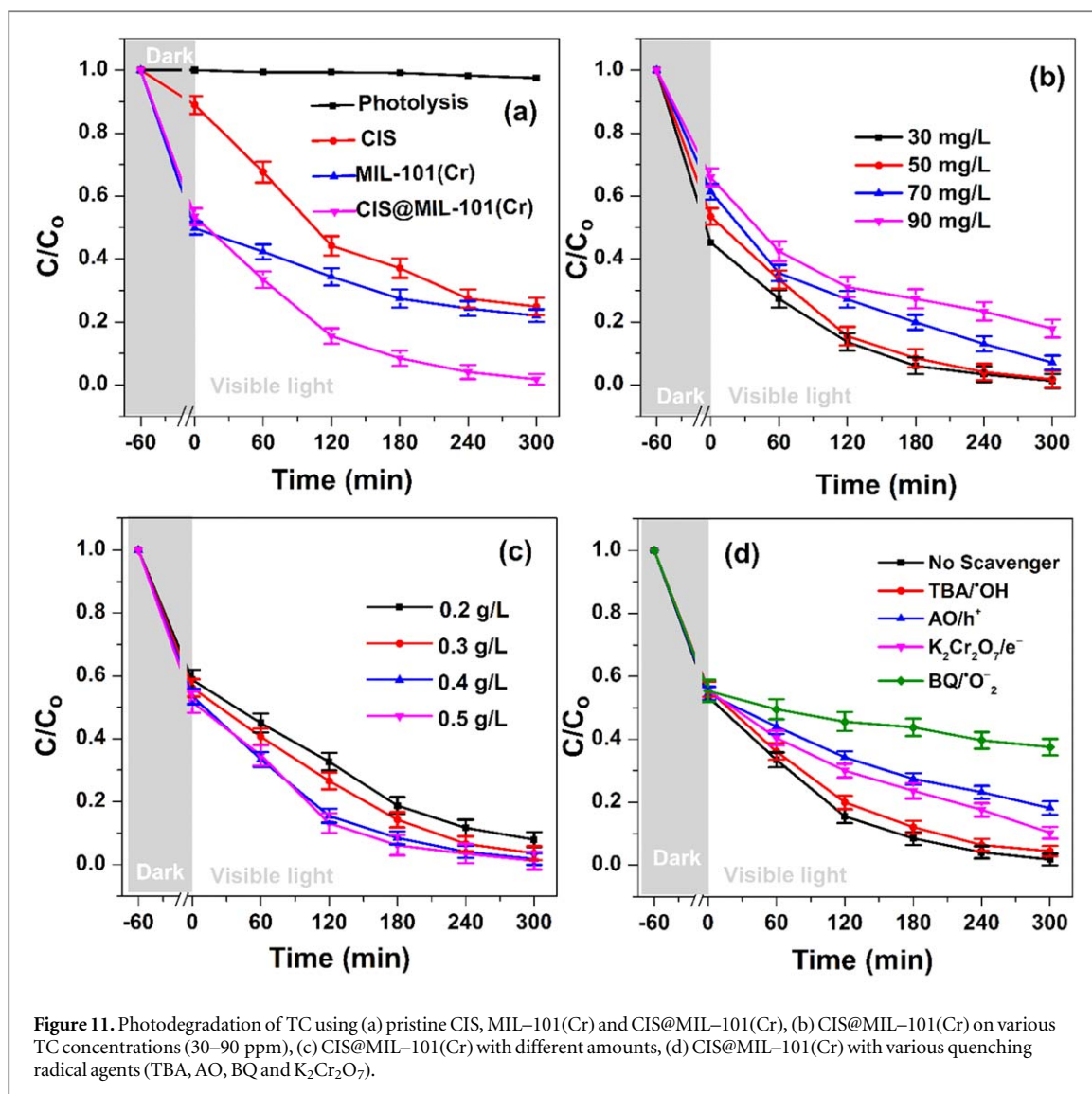


### 3.2. Photocatalytic activity tests

The photodegradation of tetracycline by CIS, MIL-101(Cr), and CIS@MIL-101(Cr) samples were investigated (figure 11(a)). The concentration of TC did not change significantly (2.5%) after 5 h of visible light irradiation without photocatalyst. The tetracycline adsorption efficiency in the dark after 60 min for CIS, MIL-101(Cr), and CIS@MIL-101(Cr) samples was 11.2%, 50.2%, and 46.5%, respectively. After 5 h of visible light irradiation, the removal efficiency of tetracycline for CIS, MIL-101(Cr), and CIS@MIL-101(Cr) samples was 75.1%, 78.0%, and 98.2%, respectively. The improved tetracycline removal efficiency of the CIS@MIL-101(Cr) composite sample compared to CIS and MIL-101(Cr) samples could be explained by the decreased recombination of electrons and holes, and a larger surface area of the composite material. These findings suggest that the presence of MIL-101(Cr) enhanced the separation efficiency of the photogenerated electrons and holes in CIS and also increased its capacity for tetracycline adsorption.



The study examined the impact of the initial tetracycline concentration and catalyst mass on the effectiveness of tetracycline removal utilizing CIS@MIL-101(Cr) as the catalyst. As shown in figure 11(b), as the initial tetracycline concentration increased from  $30 \text{ mg l}^{-1}$  to  $90 \text{ mg l}^{-1}$ , the tetracycline adsorption efficiency on CIS@MIL-101(Cr) samples decreased. Specifically, the tetracycline adsorption efficiency at concentrations of  $30 \text{ mg l}^{-1}$ ,  $50 \text{ mg /L}$ ,  $70 \text{ mg l}^{-1}$  and  $90 \text{ mg l}^{-1}$  on CIS@MIL-101(Cr) samples were 54.8%, 46.5%, 38.6% and 34.1%, respectively. The tetracycline removal efficiency on CIS@MIL-101(Cr) samples after 5 h of visible light irradiation were 98.8%, 98.2%, 92.9% and 82.1% at concentrations of  $30 \text{ mg l}^{-1}$ ,  $50 \text{ mg l}^{-1}$ ,  $70 \text{ mg l}^{-1}$  and  $90 \text{ mg l}^{-1}$ , respectively. As the initial concentration of tetracycline increased, the efficiency of its degradation decreased. This can be attributed to the higher production of intermediate compounds during the process of photodegradation, which compete with tetracycline molecules. In figure 11(c), the dose of CIS@MIL-101(Cr) photocatalyst was found to affect the efficiency of tetracycline degradation. In particular, a decrease in catalyst concentration from  $0.5 \text{ g l}^{-1}$  to  $0.2 \text{ g l}^{-1}$  resulted in a decrease in tetracycline removal efficiency from 98.7% to 92% after 300 min of light exposure. This decrease is due to the decrease in the catalyst mass and the ratio of active sites, resulting in a decrease in catalytic activity. The stability of tetracycline removal efficiency over CIS@MIL-101(Cr) was also investigated over multiple reaction cycles (figure 12). The results showed that the tetracycline removal efficiency remained almost unchanged after 4 cycles of reaction, indicating the high stability of photocatalytic activity over CIS@MIL-101(Cr) and its potential for reuse.



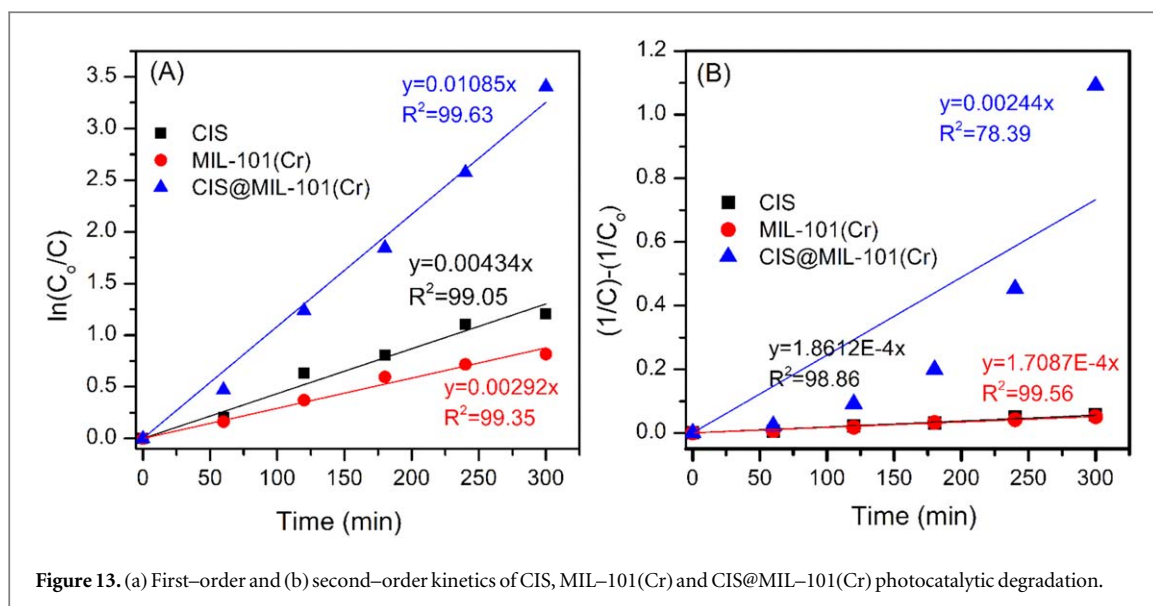


Figure 13. (a) First-order and (b) second-order kinetics of CIS, MIL-101(Cr) and CIS@MIL-101(Cr) photocatalytic degradation.

### 3.3. Kinetics and mechanism of the photocatalytic process

The pseudo-first and second-order reactions of tetracycline degradation using CIS, MIL-101(Cr), and CIS@MIL-101(Cr) photocatalysts were characterized, as shown in figure 13. The tetracycline degradation on CIS, MIL-101(Cr), and CIS@MIL-101(Cr) photocatalysts followed first-order kinetics with equations  $y = 0.00434x$  ( $R^2 = 99.05$ ),  $y = 0.00292x$  ( $R^2 = 99.35$ ), and  $y = 0.01085x$  ( $R^2 = 99.63$ ), respectively. The  $R^2$  values for all the graphs were higher than 0.99, indicating good agreement with the first-order kinetics model. On the other hand, the second-order kinetics model had lower  $R^2$  values for CIS, MIL-101(Cr), and CIS@MIL-101(Cr) photocatalysts, with equations  $y = 1.861 \times 10^{-4}x$  ( $R^2 = 98.86$ ),  $y = 1.7087 \times 10^{-4}x$  ( $R^2 = 99.56$ ), and  $y = 2.4 \times 10^{-3}x$  ( $R^2 = 78.39$ ), respectively. The results suggest that the tetracycline degradation using photocatalysts follows pseudo-first-order kinetics, and the CIS@MIL-101(Cr) photocatalyst is not suitable for the pseudo-second-order reaction.

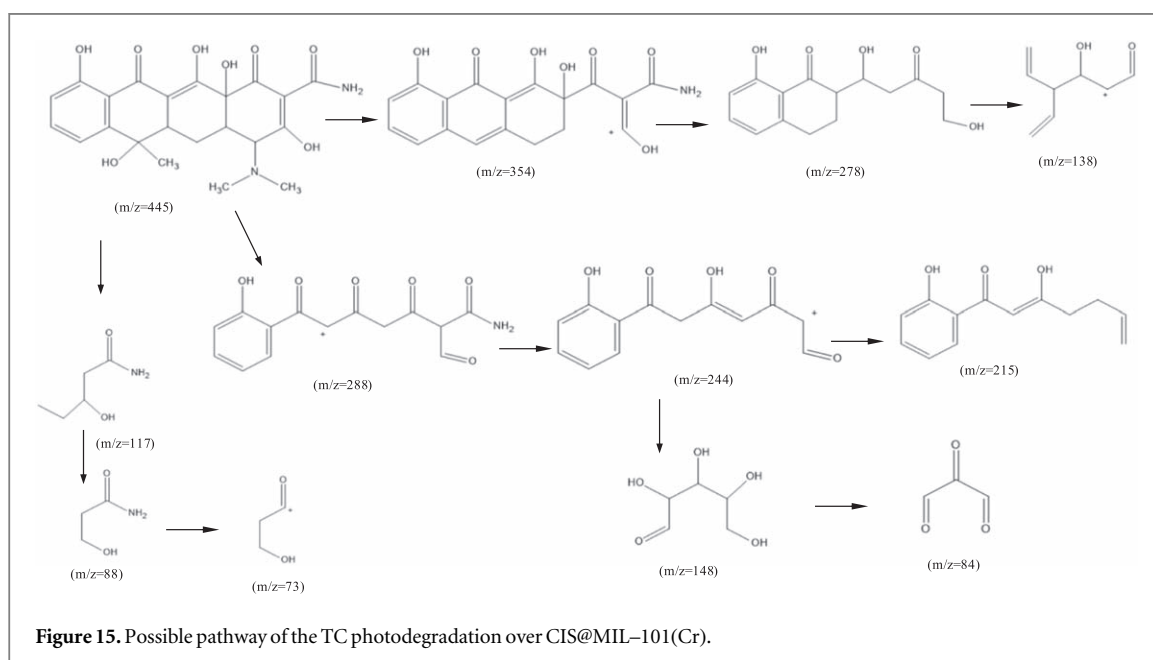
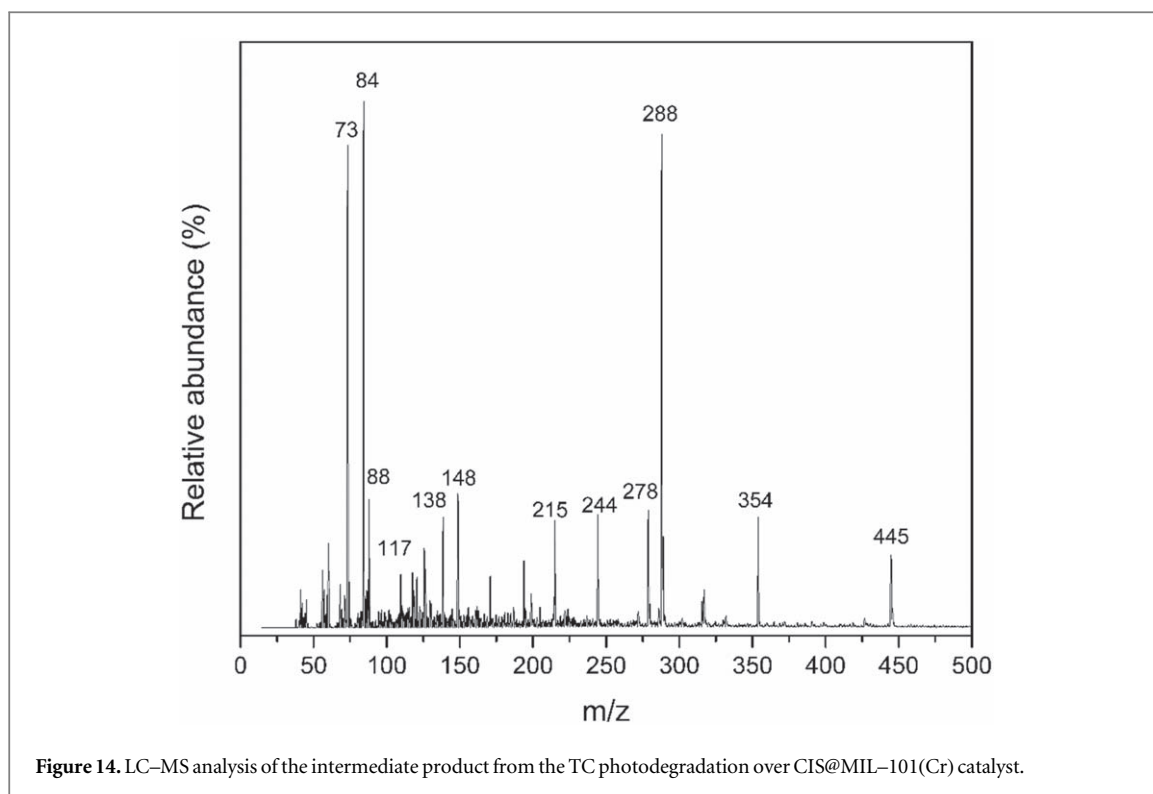
Based on the optimal conditions of CIS@MIL-101(Cr) photocatalysts, we investigated the effects of reactive species ( $\bullet\text{OH}$ ,  $\bullet\text{O}_2^-$ ), holes ( $h^+$ ) and electrons ( $e^-$ ). Radical scavengers such as *tert*-butyl alcohol (TBA), 1,4-benzoquinone (BQ), ammonium oxalate monohydrate (AO), and potassium dichromate ( $\text{K}_2\text{Cr}_2\text{O}_7$ ) were used to capture reactive species  $\bullet\text{OH}$ ,  $\bullet\text{O}_2^-$ ,  $h^+$  and  $e^-$ , respectively. In figure 11(d), it can be seen that tetracycline removal efficiency reached 98.2% without the use of reactive radical scavengers. However, when  $\text{K}_2\text{Cr}_2\text{O}_7$ , AO, and BQ were added, only 89.7%, 81.8%, and 62.5% of tetracycline were removed after 300 min of light irradiation. In contrast, after adding TBA, the removal efficiency of tetracycline reached 95.56% after 300 min of reaction. Therefore, the degradation efficiency of TC was significantly reduced and inhibited when  $\text{K}_2\text{Cr}_2\text{O}_7$ , AO, and BQ were added, indicating that  $e^-$ ,  $h^+$  and  $\bullet\text{O}_2^-$  were the dominant reactive species, and  $\bullet\text{O}_2^-$  played the most important role in the photodegradation of tetracycline on CIS@MIL-101(Cr) photocatalyst.

The intermediate products of TC photodegradation over CIS@MIL-101(Cr) were analyzed by liquid chromatography-mass spectrometry (LC-MS) (figure 14), and the photodegradation mechanism was proposed as follows: under the effect of the CIS@MIL-101(Cr) photocatalyst, a superoxide anion radical ( $\bullet\text{O}_2^-$ ) attacks several active sites on TC, generating multiple random fragmentation directions (see figure 15). These directions include the separation of hydroxyl, amine, and amide groups, as well as ring fragmentation. In the initial pathway, the removal of *N*-dimethyl and amide groups, along with the opening of the ring, produced a product that exhibited peaks at  $m/z = 354$ , 278, and 138. Another ring-opening process resulted in peaks at  $m/z = 288$ , 244, 215, and 148, 84, which correspond to compounds obtained by cleaving the ring, along with hydroxylation and oxidation. The smaller intermediate product (peaks at 117, 88, and 73) was completely degraded to  $\text{CO}_2$  and  $\text{H}_2\text{O}$  under visible light irradiation.

## 4. Conclusions

In conclusion, this study successfully demonstrated the synthesis of CIS@MIL-101(Cr) nanocomposites using waste PET as a sustainable route for material synthesis. The structural and physical properties of the nanocomposites were characterized, including the integration of  $\text{CuInS}_2$  with MIL-101(Cr) and the determination of a low band gap energy for photocatalytic activity under high visible light. The photocatalytic activity of the CIS@MIL-101(Cr) nanocomposites towards the degradation of tetracycline was found to be more





efficient and durable compared to pure CIS nanoparticles. The degradation efficiency of TC reached 98.2% after 5 h of visible light irradiation. The photocatalytic mechanism was proposed based on the analysis of intermediate products using HPLC-MS. The study also investigated the effects of various factors such as initial TC concentration, catalyst dosage, and reactive species on the degradation efficiency of TC. Moreover, the study of the photocatalytic activity revealed the kinetics and mechanism of the degradation process and the effects of reactive species, holes, and electrons were investigated using radical scavengers. The kinetics of the photocatalytic reaction was found to follow first-order kinetics, and the effects of reactive species were investigated using radical scavengers. The reactive species  $\cdot\text{O}_2^-$ ,  $h^+$ , and  $e^-$  were found to be the dominant species responsible for the photocatalytic degradation of TC. These findings provide insights into the development of new and sustainable routes for material synthesis and the potential application of CIS@MIL-101(Cr) nanocomposites in environmental remediation.

## Data availability statement

All data that support the findings of this study are included within the article (and any supplementary files).

## Declaration of competing interest

The authors declare that they have no known competing financial interests or personal relationships that could have appeared to influence the work reported in this paper.

## CRedit authorship contribution statement

Hong Van T Nguyen: Methodology, Investigation, Writing—original draft. Manh B Nguyen: Methodology, Investigation. Huan V Doan: Investigation, Writing—review & editing. Xuan Nui Pham: Conceptualization, Writing—review & editing, Supervision.

## ORCID iDs

Huan V Doan  <https://orcid.org/0000-0002-8757-364X>

Xuan Nui Pham  <https://orcid.org/0000-0002-7469-3001>

## References

- [1] Amangelsin Y, Semenova Y, Dadar M, Aljofan M and Bjørklund G 2023 The impact of tetracycline pollution on the aquatic environment and removal strategies *Antibiotics*. **12** 1–15
- [2] Daghrrir R and Drogui P 2013 Tetracycline antibiotics in the environment: a review *Environ. Chem. Lett.* **11** 209–27
- [3] Fiaz A, Zhu D and Sun J 2021 Environmental fate of tetracycline antibiotics: degradation pathway mechanisms, challenges, and perspectives *Environmental Sciences Europe*. **33** 64
- [4] Hosseinpour-Mashkani S M, Salavati-Niasari M and Mohandes F 2014 CuInS<sub>2</sub> nanostructures: Synthesis, characterization, formation mechanism and solar cell applications *J. Ind. Eng. Chem.* **20** 3800–7
- [5] Li L, Pandey A, Werder D J, Khanal B P, Pietryga J M and Klimov V I 2011 Efficient synthesis of highly luminescent copper indium sulfide-based core/shell nanocrystals with surprisingly long-lived emission *J. Am. Chem. Soc.* **133** 1176–9
- [6] Han W, Yi L, Zhao N, Tang A, Gao M and Tang Z 2008 Synthesis and shape-tailoring of copper sulfide/indium sulfide-based nanocrystals *J. Am. Chem. Soc.* **130** 13152–61
- [7] Choi S H, Kim E G and Hyeon T 2006 One-pot synthesis of copper-indium sulfide nanocrystal heterostructures with acorn, bottle, and larva shapes *J. Am. Chem. Soc.* **128** 2520–1
- [8] Fakhri H, Mahjoub A R and Khavar A H C 2014 Synthesis and characterization of ZnO/CuInS<sub>2</sub> nanocomposite and investigation of their photocatalytic properties under visible light irradiation *Appl. Surf. Sci.* **318** 65–73
- [9] Kuo K T, Liu D M, Chen S Y and Lin C C 2009 core-shell CuInS<sub>2</sub>/ZnS quantum dots assembled on short ZnO nanowires with enhanced photo-conversion efficiency *J. Mater. Chem.* **19** 6780–8
- [10] Yin Z, Hu Z, Ye H, Teng F, Yang C and Tang A 2014 One-pot controllable synthesis of wurtzite CuInS<sub>2</sub> nanoplates *Appl. Surf. Sci.* **307** 489–94
- [11] Yang F, Kuznetsov V, Lublow M, Merschjann C, Steigert A, Klaer J, Thomas A and Schedel-Niedrig T 2013 Solar hydrogen evolution using metal-free photocatalytic polymeric carbon nitride/CuInS<sub>2</sub> composites as photocathodes *J. Mater. Chem. A* **1** 6407–15
- [12] Dhakshinamoorthy A, Li Z and Garcia H 2018 Catalysis and photocatalysis by metal organic frameworks *Chem. Soc. Rev.* **47** 8134–72
- [13] Li Y, Xu H, Ouyang S and Ye J 2016 Metal-organic frameworks for photocatalysis *Phys. Chem. Chem. Phys.* **18** 7563–72
- [14] Nasalevich M A, Van Der Veen M, Kapteijn F and Gascon J 2014 Metal-organic frameworks as heterogeneous photocatalysts: advantages and challenges *Cryst. Eng. Comm.* **16** 4919–26
- [15] Ren J, Dyosiba X, Musyoka N M, Langmi H W, North B C, Mathe M and Onyango M S 2016 Green synthesis of chromium-based metal-organic framework (Cr-MOF) from waste polyethylene terephthalate (PET) bottles for hydrogen storage applications *Int. J. Hydrogen Energy* **41** 18141–6
- [16] Guo F, Yang S, Liu Y, Wang P, Huang J and Sun W Y 2019 Size engineering of metal-organic framework MIL-101(Cr)-Ag hybrids for photocatalytic CO<sub>2</sub> reduction *ACS Catal.* **9** 8464–70
- [17] Wen M, Mori K, Kamegawa T and Yamashita H 2014 Amine-functionalized MIL-101(Cr) with imbedded platinum nanoparticles as a durable photocatalyst for hydrogen production from water *Chem. Commun.* **50** 11645–8
- [18] Chen J, Zhang X, Shi X, Bi F, Yang Y and Wang Y 2020 Synergistic effects of octahedral TiO<sub>2</sub>-MIL-101(Cr) with two heterojunctions for enhancing visible-light photocatalytic degradation of liquid tetracycline and gaseous toluene *J. Colloid Interface Sci.* **579** 37–49
- [19] Sakthivel R, Pradhan K C, Nayak B B, Dash T, Sahu R K and Mishra B K 2017 Effect of fusion mixture treatment on the surface of low grade natural ruby *Appl. Surf. Sci.* **403** 267–73
- [20] Chao D, Wang L, Shen W and Guo S 2019 Effects of the lateral sizes and basal plane structure of graphene on the electrochemical properties of LiCoO<sub>2</sub> *J. Alloys Compd.* **785** 557–62
- [21] El-Sayed E S M and Yuan D 2020 Waste to MOFs: Sustainable linker, metal, and solvent sources for value-added MOF synthesis and applications *Green Chem.* **22** 4082–104
- [22] Bool R J A, Luwalhati G C, Tan N E Y, Aquino A P and Maalihan R D 2022 On the use of metal-organic framework-based adsorbent from recycled PET bottles for Eriochrome Black T removal *Mater. Today Proc.* **65** 3312–20
- [23] Manju, Kumar Roy P, Ramanan A and Rajagopal C 2013 Post consumer PET waste as potential feedstock for metal organic frameworks *Mater. Lett.* **106** 390–2

- [24] Dermanaki Farahani S and Zolgharnein J 2022 Sulfate removal by barium-terephthalate MOF synthesized from recycled PET-waste using doehlert design optimization *Inorg. Chem. Commun.* **140** 109388
- [25] Van Le D, Nguyen M B, Dang P T, Lee T and Nguyen T D 2022 terephthalic acid obtained from waste plastic for the photocatalytic degradation of the chemical warfare agent simulant, methyl paraoxon † *RSC Adv.* **12** 22367–76
- [26] Giang P T T, Hoa V T, Van N T, Quyen P T, Quang N K and Manh N B 2023 Synthesis and characterization of bimetallic Ni-Cu-BDC from waste plastic as a highly efficient CO<sub>2</sub>/N<sub>2</sub> selective adsorbent *Vietnam Journal of Chemistry.* **61** 84–9
- [27] Heidariramsheh M, Dabbagh M M, Mahdavi S M and Beitollahi A 2021 Morphology and phase-controlled growth of CuInS<sub>2</sub> nanoparticles through polyol based heating up synthesis approach *Mater. Sci. Semicond. Process.* **121** 105401
- [28] Doan H V, Nguyen H T, Ting V P, Guan S, Eloi J C, Hall S R and Pham X N 2021 Improved photodegradation of anionic dyes using a complex graphitic carbon nitride and iron-based metal-organic framework material *Faraday Discuss.* **231** 81–96
- [29] Pham X N, Vu V T, Nguyen H V T, Nguyen T T B and Doan H V 2022 Designing a novel heterostructure AgInS<sub>2</sub>@MIL-101(Cr) photocatalyst from PET plastic waste for tetracycline degradation *Nanoscale Advances.* **4** 3600–8
- [30] Zhou X, Huang W, Shi J, Zhao Z, Xia Q, Li Y, Wang H and Li Z 2014 A novel MOF/graphene oxide composite GrO@MIL-101 with high adsorption capacity for acetone *J. Mater. Chem. A* **2** 4722–30
- [31] Sheikh Alivand M, Hossein Tehrani N H M, Shafiei-Alavijeh M, Rashidi A, Kooti M, Pourreza A and Fakhraie S 2019 Synthesis of a modified HF-free MIL-101(Cr) nanoadsorbent with enhanced H<sub>2</sub>S/CH<sub>4</sub>, CO<sub>2</sub>/CH<sub>4</sub>, and CO<sub>2</sub>/N<sub>2</sub> selectivity *J. Environ. Chem. Eng.* **7** 102946
- [32] Guan R, Wang X and Sun Q 2015 Structural and optical properties of CuInS<sub>2</sub> thin films prepared by magnetron sputtering and sulfurization heat treatment *J. Nanomater.* **2015** 579489
- [33] Donohue M D and Aranovich G L 1998 Classification of Gibbs adsorption isotherms *Adv. Colloid Interface Sci.* **76–77** 137–52
- [34] Nguyen M B, Le G H, Duy T, Nguyen Q K, Trang T, Pham T, Lee T and Vu T A 2021 Bimetallic Ag-Zn-BTC/GO composite as highly efficient photocatalyst in the photocatalytic degradation of reactive yellow 145 dye in water *J. Hazard. Mater.* **420** 126560
- [35] Nguyen M B, Hong Nhung V T, Thu V T, Ngoc Nga D T, Pham Truong T N, Giang H T, Hai Yen P T, Phong P H, Vu T A and Ha V T T 2020 An electrochemical sensor based on copper-based metal-organic framework-reduced graphene oxide composites for determination of 2,4-dichlorophenol in water *RSC Adv.* **10** 42212–20
- [36] Quan X, Sun Z, Meng H, Han Y, Wu J, Xu J, Xu Y and Zhang X 2019 Surface functionalization of MIL-101(Cr) by aminated mesoporous silica and improved adsorption selectivity toward special metal ions *Dalton Trans.* **48** 5384–96
- [37] Xie B B, Bin Hu B, Jiang L F, Li G and Du Z L 2015 The phase transformation of CuInS<sub>2</sub> from chalcopyrite to wurtzite *Nanoscale Res. Lett.* **10** 86
- [38] Lei S, Wang C, Liu L, Guo D, Wang C, Tang Q, Cheng B, Xiao Y and Zhou L 2013 Spinel indium sulfide precursor for the phase-selective synthesis of Cu-In-S nanocrystals with zinc-blende, wurtzite, and spinel structures *Chem. Mater.* **25** 2991–7
- [39] Li Z, Zhang H, Zha Q, Zhai C, Li W, Zeng L and Zhu M 2020 Photo-electrochemical detection of dopamine in human urine and calf serum based on MIL-101(Cr)/carbon black *Microchim. Acta* **187** 526
- [40] Wu S M, Xue Y Z, Zhou L M, Liu X and Xu D Y 2014 Structure and morphology evolution in mechanochemical processed CuInS<sub>2</sub> powder *J. Alloys Compd.* **600** 96–100
- [41] Makuła P, Pacia M and Macyk W 2018 How to correctly determine the band gap energy of modified semiconductor photocatalysts based on UV-vis spectra *J. Phys. Chem. Lett.* **9** 6814–7
- [42] Wang Y, Han D, Wang Z and Gu F 2023 Efficient photocatalytic degradation of tetracycline under visible light by an all-solid-state Z-scheme Ag<sub>3</sub>PO<sub>4</sub>/MIL-101(Cr) heterostructure with metallic Ag as a charge transmission bridge *ACS Appl. Mater. Interfaces* **15** 22085–100
- [43] Nguyen M B, Sy D T, Thoa V T K, Hong N T and Doan H V 2022 Bimetallic Co-Fe-BTC/CN nanocomposite synthesised via a microwave-assisted hydrothermal method for highly efficient Reactive Yellow 145 dye photodegradation *J. Taiwan Inst. Chem. Eng.* **140** 104543
- [44] Kim H J, Bae J H, Seo H, Shiratani M and Gopi C V V M 2018 ZnS/SiO<sub>2</sub> passivation layer for high-performance of TiO<sub>2</sub>/CuInS<sub>2</sub> quantum dot sensitized solar cells *Energies.* **11** 1–9
- [45] Verma P and Samanta S K 2018 Facile synthesis of TiO<sub>2</sub>-PC composites for enhanced photocatalytic abatement of multiple pollutant dye mixtures: a comprehensive study on the kinetics, mechanism, and effects of environmental factors *Res. Chem. Intermed.* **44** 1963–88
- [46] Pham G T T, Vu H T, Pham T T, Thanh N N, Thuy V N, Tran H Q, Doan H V and Nguyen M B 2023 Exploring the potential of ZnO-Ag@AgBr/SBA-15 Z-scheme heterostructure for efficient wastewater treatment: synthesis, characterization, and real-world applications *RSC Adv.* **13** 12402–10
- [47] Thi Quynh Anh N, Ngoc H M, Van Noi N and Huu Van N 2023 Enhanced photocatalytic degradation of direct blue 71 dye using TiO<sub>2</sub>-PAA-GO composite in aqueous solution *Mater. Res. Express* **10** 055503